COMPUTATIONAL ANALYSIS OF ROTOR-FUSELAGE INTERACTIONAL AERODYNAMICS USING SLIDING-PLANE CFD METHOD

R. Steijl and G. Barakos

CFD Laboratory, Department of Engineering, University of Liverpool, L63 3GH, U.K.

Abstract

Aerodynamic interactions between the main rotor, fuselage and tail rotor must be considered during the design phase of a helicopter and their effect on performance must be quantified. However, interactional helicopter aerodynamics has so far been considered by very few researchers and this is due to the geometric complexity and complex flow physics involved in the analysis of full helicopter configurations. The aim of the present work is the development of a CFD method capable of accurately simulating the flow around a full helicopter which could be used to improve understanding of helicopter interactional aerodynamics. In the present work, the Helicopter Multi-Block (HMB) flow solver[1, 2, 3] of the CFD Laboratory at Liverpool University is used to investigate the flow around two generic rotor-fuselage cases, i.e. the GeorgiaTech rotor-cylinder test case and the ROBIN rotor-fuselage test case, before moving on to a more realistic full helicopter geometry under investigation in the European Commission Framework 6 GOAHEAD project. A comparison of the results obtained using the HMB method with experimental data shows that the method is capable of resolving the main interactional flow features for the generic cases. A similar comparison for the GOAHEAD test case has not yet been conducted, but the obtained results show that even for a test case of high complexity, state-of-the-art rotorcraft CFD methods are capable of providing realistic predictions.

1 Introduction

Prediction of aerodynamic interactions between the main rotor, tail rotor and fuselage is crucial for performance analysis of helicopter configurations. Regardless of its importance, interactional helicopter aerodynamics has so far been considered by few researchers due to a number of reasons. First, the aero-mechanics of an isolated rotor is still a very challenging area, since it constitutes a complex multi-disciplinary problem involving vortical wake flows, transonic flow regions, rotor blade dynamics and elastic blade deformation. Naturally, understanding interactional helicopter aerodynamics requires a good level of understanding of rotor aero-mechanics. The second reason for the limited number of studies in interactional aerodynamics is the geometric complexity and even more complex flow physics involved in rotor-fuselage or full helicopter configurations. Therefore, most of the published works concern wind tunnel experiments with generic helicopter rotors mounted over idealised fuselage shapes, e.g. the rotor-cylinder test case of GeorgiaTech [4, 5] and the ROBIN test case of NASA [6, 7, 8]. In the first example, the airframe is represented by a circular cylinder with hemispherical nose, while the ROBIN case is closer to a helicopter fuselage shape, but tail planes, engine inlets, exhausts, etc. are ignored.

The importance of helicopter interactional aerodynamics, combined with the progress in CFD algorithms and the availability of powerful affordable computers, encouraged a few recent CFD studies [9, 10, 11, 12, 13, 2]. These investigations have not yet reached the maturity of numerical investigations of hovering rotors or isolated rotors in forward flight and there are a number of contributing factors for this. At first, the geometric complexity of a rotor-fuselage or a full helicopter configuration is high, and the resulting task to generate good quality CFD meshes is challenging. In addition, the complexity of CFD methods capable of solving the flow around a helicopter is increased, due to the need to handle relative motions of rotor blades and fuselages. Finally, a third major factor is the lack of adequate wind tunnel flight test data for validation purposes.

Therefore, an urgent need exists for a database of high quality experimental data, which can act as validation for the state-of-the-art CFD methods. To address this need, the European Commission funded the Framework 6 Program GOAHEAD, with the aim to create such an experimental data base and to validate state-of-the-art CFD methods. The CFD Laboratory at Liverpool University is involved in the CFD work package of this project, using the Helicopter Multi-Block (HMB) flow solver [1, 2]. The Helicopter Multi-Block (HMB) solver uses a sliding-grid technique to handle the rela-

tive motion of the rotor(s) and the helicopter fuselage. The CFD package comprises a pre-wind tunnel test phase, in which the partners provide CFD results using predicted test conditions, and a post-wind tunnel test phase, during which the wind tunnel results are available. The CFD results for the blind pre-wind tunnel test phase were presented in Ref.[14].

The present paper is structured as follows. First, a review of published experimental numerical investigations into helicopter interactional aerodynamics is presented in Section 2. Then, the CFD method used in the present study is described in Section 3. Section 4 presents the results for the Georgia Tech teetering rotor test case, while the ROBIN rotor-body test case is described in Section 5. Results for the NH90-like geometry under investigation in the GOAHEAD project are presented in Section 6. Finally, conclusions are drawn in Section 7, along with future research plans.

2 Review of previous work

In the present work, the well-known GeorgiaTech rotor-cylinder interaction experimental data is used both for validation of the present CFD method and the analysis of interactional aerodynamics of simple fuselage shapes. In the GeorgiaTech experiments, a simple two-bladed teetering rotor is considered mounted on a cylindrical airframe with hemispherical node. The surface pressure measurements for this series of experiments were presented by Brand, McMahon and Komerath [4]. Velocity field measurements for this configuration were also presented in the late eighties by Liou, Komerath and McMahon [15, 16].

In their work, Kim and Komerath [5] presented a summary of experimental works for the interaction of the wake of simple two-bladed rotors with a cylindrical airframe. In addition, they presented comparisons of the experimental results with results from theoretical modelling of the interaction. The paper described the differences between the wake/fuselage interaction at the front of the rotor disk with that at the aft part. Building on potential flow models, the authors describe the wake-fuselage interaction in two phases, i.e. a pre-collision phase in which the wake vortex trajectory is modified by the presence of the fuselage and a collision phase dominated by complex vortex-boundary layer interactions. The pre-collision phase can be modelled with potential flow theory while the collision phase obviously requires viscous flow models. The forward shaft tilt in the rotor-cylinder test cases was also considered and the closer proximity of the rotor and the cylinder at the front of the disk, as compared to the separation of the rotor disk from the cylinder at the back, led to a qualitatively different behaviour of the vortex path. In the theoretical model discussed by Kim and Komerath [5], the vortex wake descent is significantly decelerated relative to the isolated rotor wake development at the front of the rotor disk, while the deceleration is absent at the back. In the potential flow model, the interaction with the cylinder is different due to the opposite sense of vortex rotation at the front and back of the rotor disk, i.e. at the front of the disk, the vortex can be expected to proceed directly to collide with the surface, while at the back, the vortex can be expected to have a less direct interaction, as it travels along the surface. Naturally, vortex-boundary layer interactions will play an important role, particularly when the interaction leads to flow separation on the cylinder/fuselage. This set of results and observations highlights the difficulty in developing theoretical models for wake-fuselage interaction. In more recent studies, models including viscous effects have been discussed by Affes and co-workers [17, 18].

CFD investigations of the rotor-cylinder interaction have been presented previously by various researchers. An early numerical investigation based on potential flow methods was presented by Komerath and co-workers [19]. More recent works include research efforts in which the rotor effect is modelled using an actuator disk, and CFD investigations using full simulation of the time-dependent rotor-cylinder problem with moving rotor meshes. The latter category mainly involves works based on overset mesh methods, the work of Hariharan and Sankar [20] is a good example. Park and Kwon [10] also presented results using a sliding-plane method with unstructured meshes. Interestingly, the predictions based on the Euler equations by both Hariharan and Sankar [20] and Park and Kwon [10] under-predict the peak in averaged pressure present at the back of the rotor disk relative to the experimental data.

3 Sliding-plane CFD method

The Helicopter Multi-Block (HMB) CFD code [1, 2, 3, 13] was employed for this work. HMB solves the unsteady Reynolds-averaged Navier-Stokes equations on block-structured grids using a cell-centred finite-volume method for spatial discretisation. Implicit time integration is employed, and the resulting linear systems of equations is solved using a pre-conditioned Generalised Conjugate Gradient method. For unsteady simulations, an implicit dual-time stepping method is used, based on Jameson's pseudo-time integration approach [21]. The method has been validated for a wide range of aerospace applications and has demonstrated good

accuracy and efficiency for very demanding flows. Examples of work with HMB can be found in references [1, 2, 13, 22, 23, 24]. Several rotor trimming methods are available in HMB along with a blade-actuation algorithm that allows for the near-blade grid quality to be maintained on deforming meshes [1].

The HMB solver has a library of turbulence closures which includes several one- and two- equation turbulence models and even non-Boussinesq versions of the $k-\omega$ model. Turbulence simulation is also possible using either the Large-Eddy or the Detached-Eddy approach. The solver was designed with parallel execution in mind and the MPI library along with a load-balancing algorithm are used to this end. For multi-block grid generation, the ICEM-CFD Hexa commercial meshing tool is used and CFD grids with 10-20 million points and thousands of blocks are commonly used with the HMB solver.

The underlying idea behind the sliding-mesh approach can be explained using Figure 1 which shows the definition of two layers of halo cells around the boundary surface of each block. In the sliding plane algorithm, this concept is extended to deal with grids which are discontinuous across the interface and can also be in relative motion. Figure 1(b) presents a situation where two adjacent blocks have non-matching cell faces. If the halo cells of each block are populated with interpolated values of the flow field variables, the solver will have no difficulty in updating the flow solution. The application of the sliding-plane algorithm to non-matching grids as well as grids in relative motion will result in non-matching cell faces as sketched in Figure 1(b). There are three main steps involved in populating the halo cells: i) identification of the neighbouring cells for each halo-cell, ii) interpolation of the solution at the centroids of the halo cells and iii) exchange of information between blocks associated with different processors. The last step is important for computations on distributed-memory machines only. Regardless of the identification and interpolation methods employed, the halo-cell values are computed using:

$$\phi_{halo} = \sum_{i=1}^{i=n} w_i \phi_i \qquad (1)$$

where ϕ represents any flow field variable, w_i is the weight associated with the ith neighbour of the halo cell and n is the number of neighbours.

The distance-based interpolation (shown in Figure 1(c)) computes a weighted sum of flow field data of neighbouring cells within an interaction radius. The weights are inversely proportional to the distance of the cell centre from the projected point on the sliding plane interface and are scaled to sum up to one. Figure 1(d) shows the cell-face overlap interpolation, in which case the weight for each neighbour is directly proportional to the fraction of the projected cell face area that overlaps with the cell face of this neighbour cell. In the context of finite-volume discretisation methods for conservation laws based on numerical fluxes through cell faces, the cell-face overlap interpolation is the preferred method. However, an interpolation method based on the overlap weighting of Figure 1(d) does not necessarily enforce conservation and due to differences in grid sizes on both sides of the sliding-plane interface may act as a spatial filter.

The present implementation of the sliding-mesh algorithm is based on the cell-face overlap interpolation method presented in Figure 1(d). Sliding-mesh interfaces can be of arbitrary shape and for this reason the contributing cell surfaces must all be projected on the curvilinear ξ, η, ζ axes as used in the present finite-volume solver. This step can be combined with a transformation from to conservative variables so that flux-weighted summations can also be computed.

4 GeorgiaTech teetering-rotor test case

The first rotor-fuselage test case considered in this work, is based on the experiments conducted at Georgia Institute of Technology for a idealised fuselage interacting with a two-bladed teetering rotor [4]. For this test case, unsteady surface pressure measurements, as well as particle-image velocimetry data are available. This availability and the low geometric complexity of the considered wind tunnel model make this a well-established test case for investigations of interactional aerodynamics and validation of CFD codes. The configuration consists of a 134mm diameter cylindrical airframe with a hemispherical nose. It is supported by a wind tunnel sting, independent of the two-bladed rotor that is driven by a shaft mounted on the wind tunnel ceiling. In the present work, the wind tunnel support for the airframe and the rotor drive shaft are neglected. Figures 3(a) and (b) show the idealised geometry considered in the present investigation. The rotor centre was located 1.0 rotor radius behind the centre of the hemispherical nose cone and 0.3 above the centre line of the airframe. The rotor is of the teetering type and the blades are untwisted with NACA0015 sections. The blade chord was 86 mm and the radius 450 mm. The grid used has a total of 514 blocks and $2.5 \cdot 10^6$ cells. The rotor grid has 324 blocks and $1.6 \cdot 10^6$ cells. The background grid containing the airframe has 190 blocks with an O-type topology around the cylindrical airframe and $0.9 \cdot 10^6$ cells. The test case has an advance

ratio of 0.10, leading to $C_T = 0.0090$. Collective and cyclic controls were eliminated in the experiment, while the rotor was mounted at a 6^o forward shaft tilt. Since, the simulations for this test case are mainly conducted to validate the present sliding-plane CFD method [2], the rotor mesh motion and deformation method used for fully articulated rotors [1] was used here as well. Therefore, in the simulations, the one-piece rotor from the experiment was replaced by a rotor with small root cut-out and a simple ellipsoidal rotor head. The far-field boundaries considered in the simulations were formed by a rectangular box. The rotor grid has flat upper and lower boundaries and a cylindrical outer boundary surface. This mesh was embedded in a cylindrical drum-shaped cavity in the stationary airframe grid. The sliding-plane method was employed on the drum-shaped surface surrounding the rotor grid, as sketched in Figures 3(c) and (d). The surface mesh for the airframe and rotor is also shown in Figure 3. In the present simulations, the first flap harmonic of the rotor was replaced by a cyclic pitch motion and modified rotor shaft inclination, using the pitch-flapping equivalence. The flapping coefficients were obtain from published works [10]. The motivation behind the removal of the flapping motion is that the close proximity of the rotor and the cylinder for $\psi = 180^o$, i.e. at the front of the rotor disk, leads to a rotor grid with a lower domain boundary close to the rotor plane. The flapping motion would therefore have given a more significant grid deformation than the equivalent pitching motion.

Figure 4 presents the chordwise surface pressure distribution at six spanwise stations of the rotor for $\psi = 0^o$, 90^o, 180^o and 270^o. The plots clearly show that the effect of the flapping of the rotor is to increase the effective blade incidence at the retreating side and the rear part of the rotor disk. The low tip Mach number of 0.295, combined with the moderate advance ratio of 0.10 resulted in subsonic flow even at the outboard stations of the advancing side. The first rotor-fuselage interactional aerodynamic effect considered here is the change in the time-averaged pressure distribution along the crown line of the cylinder compared to the steady state pressure without the rotor. Figure 5 shows the results from two Euler simulations compared to the experimental data for the averaged pressure. The figure shows two distinct peaks in pressure near the tip of the rotor blades. For this untwisted rotor, the rotor clearly carries most of the load on its outboard stations. The stagnation of the induced velocity component normal to the cylinder surface gives rise to a pressure increase. The Euler simulations obviously do not include the effects of the viscous interaction of the vortex wake of the rotor with the boundary layer on the cylinder. Also, the experimental data indicate that the flow will have separation in the nose region (where the c_p has a plateau) through at least part of the rotor revolution, an effect absent from the simulations. Figure 5 shows the effect of the flapping on the cylinder surface pressure. Consistent with the increased rotor loading on the advancing side and rear part of the rotor disk shown in Figure 4, this increased rear loading increases the surface pressure near the second peak, while the reduced loading at the front of the disk due to flapping reduces the first pressure peak. The instantaneous surface pressure along the crown of the cylinder is shown in Figure 6. The figure compares the Euler results including the blade flapping with experimental data. Figures 6(a) and (b) show the situation when the blade is passing over the nose of the cylinder, for blade azimuths of 180^o and 185^o, respectively. The simulation resolves well the sharp rise of surface pressure, considering the absence of viscous effects and the coarseness of the employed mesh. The pressure increase due to the rotor induced flow far exceeds the stagnation pressure of the freestream flow. The plots also show the strong azimuthal dependency of the instantaneous pressure, which means that a slight shift in phasing relative to the experimental data could lead to serious discrepancies with the experiment. Figures 6(c) and (d) show the pressure at blade azimuth angles of 145^o and 155^o, respectively. These correspond to 35 and 25 degrees of azimuth before the blade passage. Clearly, the induced pressures are significantly lower than before, since no direct interaction with the blade occurs.

5 ROBIN test case

A second test case considered in this paper involves the ROBIN helicopter model [6, 25, 26]. The overall configuration is shown in Figure 7(a). The four-blade rotor has an aspect ratio of 13 and consists of a NACA0012 section, with a linear twist of 8^o. In the experimental setup, the rotor was suspended from the wind tunnel roof, while the fuselage was on a floor-mounted support. Both supporting structures are omitted in the geometry used here. The rotor hub is modelled as an ellipsoidal surface. The CFD geometry includes the 2-inch rotorshaft offset from the fuselage centreline, and the 3^o forward tilt of the rotor shaft. Figure 7(b) shows the locations of the surface pressure taps and inflow flow measurements from the NASA experiments, which are used here. The test case considered had a rotor tip Mach number of 0.5, the advance ratio was 0.15 and the rotor thrust coefficient was $C_T/\sigma = 0.0656$ as in the experiment. The rotor trim state reported by Park and Kwon [9], with collective, longitudinal

and lateral cyclic pitch angles of 6.0^o, -2.2^o and -2.0^o, respectively was used. The inviscid flow simulations were conducted on multi-block structured grids with the sliding plane interface located one blade chord below the rotor disk. The grid had an O-type topology in the direct vicinity of the fuselage, embedded in a domain with a cylindrical side surface, of the same diameter as the rotor grid far-field boundary, and an upper surface orthogonal to the rotor shaft. The grid was made of 240 blocks and $4.0 \cdot 10^6$ cells. The topology and mesh are shown in Figure 7(c). The rotor grid had a C-H topology, with 456 blocks and $5.5 \cdot 10^6$ cells. The grid had 50 cells in the spanwise direction of each blade, 45 cells in the surface normal direction, 150 cells around the blade chord and 40 cells in the stream-wise direction between the blades. The simulation was run for 4 rotor revolutions using azimuthal steps of 1.0 degree. For the 4th rotor revolution, the thrust coefficient was $C_T/\sigma = 0.0066$, which is within 0.6% of the value for the 3rd revolution, indicating a sufficient level of convergence, confirmed by surface pressure plots for the 3rd and 4th revolution discussed later. The searches and interpolation weights for the sliding meshes were pre-computed as discussed in Ref.[2], requiring about 5% of the total CPU time. The sliding-plane method added an additional $5 - 6\%$ communication overhead for the parallel simulation conducted on 40 Pentium 4 processors of a Linux cluster.

Figure 8 compares the time-averaged induced flow field components in the stream-wise and rotor-disk normal direction from the experiment[7] with CFD data averaged over one rotor revolution. The agreement is favourable, with a slight over-prediction of the stream-wise component. This is an encouraging result, since any loss of continuity across the sliding plane would have an effect on the obtained velocity field.

Time-averaged surface pressure coefficients are shown in Figure 9 for the cross-sections x/L=0.35 and x/L=1.17. The small discrepancy at the lower surface for x/L=1.17 can be (partly) attributed to the absence of the wind tunnel support in the CFD geometry. Figure 10 compares the predicted time-dependent surface pressure coefficients with the experimental data[26]. The pressure at the four centreline positions defined in Figure 7(b) is shown in Figures 11(a)-(d). The pressure at probe locations on the side of the fuselage fairing is shown in Figures 11(a) and (b), for the retreating and advancing side of the rotor, respectively. The peak-to-peak pressure fluctuations agree favourably with the experiment and the results of Park and Kwon [9], which are shown here for comparison.

6 GOAHEAD rotor-fuselage test case

A second rotor-fuselage test case demonstrates the capability of the method to handle complex, realistic helicopter geometries. The case considered here is the wind-tunnel model of a medium-weight generic helicopter with the 4-bladed ONERA 7AD rotor, equipped with anhedral tips and parabolic taper, and the BO105 2-bladed tail rotor. This configuration is under investigation for the GOAHEAD EC 6th Framework Research Project. Figure 12 shows the geometry and the multi-block structured mesh used for the Reynolds-Averaged Navier-Stokes simulations. For this full helicopter geometry, the main and tail rotors are placed within a drum-shaped sliding-plane interface, as shown in Figure12(a-b). The close proximity of the main and tail rotor planes are notable in the figure, which leads to an additional challenge in the generation of the multi-block structured meshes used here. The main rotor drum has the forward tilt of the main rotor shaft, while the tail rotor drum is tilted about the x-axis as well as the z-axis (in the tail rotor, hub-centred coordinate system) to provide a small forward and upward thrust component. The multi-block mesh used here, consists of 3786 blocks and approximately $27 \cdot 10^6$ cells. The mesh in the $y = 0$ plane is shown in Figures 12(c-e). The case considered corresponds to an economic cruise condition, for which the free-stream Mach number is 0.204 and the tip Mach number of the rotor 0.62. A representative rotor trim schedule is used in the simulation, i.e. the rotor has cyclic pitch change as well as a harmonic blade flapping. The multi-block topology of the rotors is designed to handle the grid deformation as discussed in Ref.[1]. This test case was run on the Hector supercomputer at EPCC in Edinburgh. The simulation was run for three rotor revolutions with a time-step corresponding to 0.25^o of main rotor rotation. The $k-\omega$ turbulence model was used.

Figure 13(a) shows the instantaneous surface pressure distribution at a main rotor azimuth of 90^o during the third revolution (economic cruise conditions, $\mu = 0.3$). The effect of the blade passing on the surface pressure distribution on the front part of the fuselage is shown in detail in Figure 13(b), where the $x = 0.75$ plane is shown. The main rotor blade passing through the front of the rotor disk clearly induces a (delayed) pressure rise on the forward fuselage, as discussed previously in Ref. [2]. The interaction of the tail rotor with the fin is shown in Figure 13(c), showing the c_p contours in the $z = 0.775$ cross section. The tail rotor blade is at $\psi = 0^o$, which corresponds to the downward vertical position. For the rotation direction of the tail rotor used here, this position is in the

retreating side of the tail rotor disk. The blade stagnation pressure in the selected cross-section is therefore only around twice the fin stagnation pressure. In addition to the direct impulsive effect, the tail rotor-fin interaction also includes the effect of the tail rotor induced velocity on the flow around the side-force generating fin, by effectively changing the flow angle in a time-periodic fashion. This effect is more difficult to analyse than the pressure impulse effect show in the figure. A comparison of simulation results with and without tail rotor would clearly show this contribution.

7 Conclusions

A computational analysis of helicopter interactional aerodynamics is currently under way at the CFD Laboratory at the University of Liverpool. The present paper showed results obtained using the HMB CFD method, which has been extended with a sliding-mesh algorithm enabling simulations of flows around full helicopter configurations. A comparison of the results obtained using the HMB method with experimental data shows that the method is capable of resolving the main interactional flow features for the generic cases. A similar comparison for the GOAHEAD test case has not yet been conducted, but is planned for the near future in the framework of the European Union Framework 6 GOAHEAD project. The results obtained for the GOAHEAD test case show the capability of the CFD method to handle flow simulations for complex helicopter configuration in demanding flight conditions.

Acknowledgements
During this work, R. Steijl was supported by the European Union under the Integrating and Strengthening the European Research Area Programme of the 6th Framework, Contract Nr.516074 (GOAHEAD project). Some of the computations presented in this paper were carried out using the Hector super-computer of the UK under the EPSRC grant EP/F005954/1.

References

[1] R. Steijl, G.N. Barakos, and K.J. Badcock. A Framework for CFD Analysis of Helicopter Rotors in Hover and Forward Flight. *Int. J. Numer. Meth. Fluids*, 51:819–847, 2006.

[2] R. Steijl and G.N. Barakos. Sliding Mesh Algorithm for CFD Analysis of Helicopter Roto-Fuselage Aerodynamics. accepter for publication in Int. J. Numer. Meth. Fluids, December, 2007.

[3] K.J. Badcock, B.E. Richards, and M.A. Woodgate. Elements of computational fluid dynamics on block structured grids using implicit solvers. *Progress in Aerospace Sciences*, 36:351–392, 2000.

[4] A.G. Brand, H.M. McMahon, and N.M. Komerath. Surface Pressure Measurements on a Body Subject to Vortex Wake Interaction. *AIAA journal*, 27(5), 1989.

[5] J.M. Kim and N.M. Komerath. Summary of the interaction of a Rotor Wake with a Circular Cylinder. *AIAA journal*, 33(3), 1995.

[6] C.E. Freeman and R.E. Mineck. Fuselage Surface Pressure Measurements of a Helicopter Wind-Tunnel Model with a 3.15-Meter Diameter Single Rotor. Technical Report TM-80051, NASA, 1979.

[7] J.W. Elliott, S.L. Althoff, and R.H. Sailey. Inflow Measurements Made With a Laser Velocimeter on a Helicopter Model in Forward Flight - Volume I: Rectangular Planform Blades at an Advance Ratio of 0.15. Technical Report TM-100541, NASA, 1988.

[8] J.W. Elliott, S.L. Althoff, and R.H. Sailey. Inflow Measurements Made With a Laser Velocimeter on a Helicopter Model in Forward Flight - Volume II: Rectangular Planform Blades at an Advance Ratio of 0.23. Technical Report TM-100541, NASA, 1988.

[9] Y. Park, H.J. Nam, and O.J. Kwon. Simulation of unsteady rotor-fuselage aerodynamic interaction using unstructured adaptive meshes. American Helicopter Society 59th Annual Forum, Phoenix, Arizona, May 6-8., 2003.

[10] Y. Park and O. Kwon. Simulation of unsteady rotor flow field using unstructured adaptive sliding meshes. *J. American Helicopter Society*, 49(4):391–400, 2004.

[11] H.J. Nam, Y. Park, and O.J. Kwon. Simulation of unsteady rotor-fuselage aerodynamic interaction using unstructured adaptive meshes. *J. American Helicopter Society*, 51(2):141–148, 2006.

[12] T. Renaud, C. Benoit, J.-C. Boniface, and P. Gardarein. Navier-stokes computations of a complete helicopter configuration accounting for main and tail rotor effects. 29th European Rotorcraft Forum, Friedrichshafen, Germany, September, 2003.

[13] G. Barakos, R. Steijl, K. Badcock, and A. Brocklehurst. Development of CFD Capability for Full Helicopter Engineering Analysis. 31st European Rotorcraft Forum, 13-15 September 2005, Florence, Italy, 2005.

[14] O. Boelens, G. Barakos, M. Biava, A. Brocklehurst, M. Costes, A. D'Alascio, M. Dietz, D. Drikakis, J. Ekatarinaris, I. Humby, W. Khier, B. Knutzen, F. Le Chuiton, K. Pahlke, T. Renaud, T. Schwarz, R. Steijl, L. Sudre, L. Vigevano, and B. Zhong. The Blind-Test Activity of the GOAHEAD Project. 33rd European Rotorcraft Forum, Kazan, Russia, September, 2007.

[15] S.G. Liou, N.M. Komerath, and H.M. McMahon. Velocity Measurements of Airframe Effects on a Rotor in Low-Speed Forward Flight. *AIAA journal*, 26(4), 1988.

[16] S.G. Liou, N.M. Komerath, and H.M. McMahon. Velocity Field of a Cylinder in the Wake of a Rotor in Forward Flight. *AIAA journal*, 27(9), 1989.

[17] H. Affes, A.T. Conlisk, J.M. Kim, and N.M. Komerath. Model for Rotor Tip Vortex-Airframe Interaction, Part 2: Comparison with Experiment, Vortex Wake Interaction. *AIAA journal*, 31(12), 1993.

[18] H. Affes, Z. Xiao, A.T. Conlisk, J.M. Kim, and N.M. Komerath. Model for Rotor Tip Vortex-Airframe Interaction, Part 3: Viscous Flow on Airframe, Vortex Wake Interaction. *AIAA journal*, 36(3), 1998.

[19] N.M. Komerath, D.M. Mavris, and S.G. Liou. Prediction of Unsteady Pressure and Velocity over a Rotorcraft in Forward Flight. *Journal of Aircraft*, 28(8), 1991.

[20] N. Hariharan and L.N. Sankar. Unsteady Overset Simulation of Rotor-Airframe Interaction, Circular Cylinder. *AIAA journal*, 40(4), 2003.

[21] A. Jameson. Time Dependent Calculations Using Multigrid, with Applications to Unsteady Flows past Airfoils and Wings. AIAA Paper 1991-1596, 10th Computational Fluid Dynamics Conference , Honolulu, Hawai, June 24-26, 1991.

[22] R. Morvant, K.J. Badcock, G.N. Barakos, and B.E. Richards. Aerofoil-Vortex Interaction Using the Compressible Vorticity Confinement Method. *AIAA J.*, 43(1):63–75, 2004.

[23] A. Spentzos, G. Barakos, K. Badcock, B.E. Richards, P. Wernert, S. Schreck, and M. Raffel. CFD Investigation of 2D and 3D Dynamic Stall. *AIAA J.*, 34(5):1023–1033, 2005.

[24] R. Steijl and G.N. Barakos. A Computational Study of the Advancing Side Lift Phase Problem. *Journal of Aircraft*, 45(1):246–257, 2008.

[25] M.S. Chaffin and J.D. Berry. Navier-Stokes and Potential Theory Solutions for a Helicopter Fuselage and Comparison with Experiment. Technical Report TM-4566, NASA, 1994.

[26] R.E. Mineck and S. Althoff Gorton. Steady and Periodic Pressure Measurements on a Generic Helicopter Fuselage Model in the Presence of a Rotor. Technical Report TM-2000-210286, NASA, 2000.

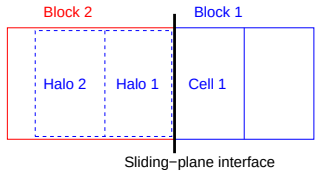

(a) Halo cells and matching cells

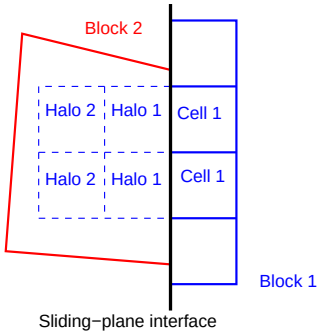

(b) Non-matching cells along interface

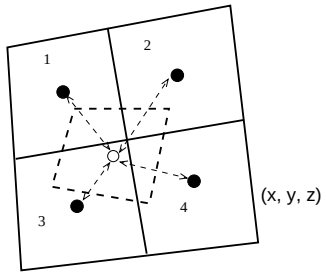

(c) Distance-based interpolation

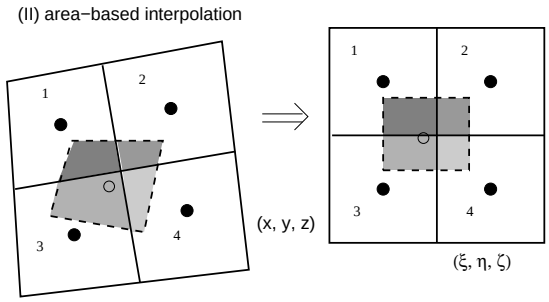

(d) Face area-based interpolation

Figure 1: Sliding plane interface with matching and non-matching cell faces. (a) matching halo cells, (b) non-matching interface, (c) sketch of distance-based interpolation, (d) sketch of cell-area weighted interpolation.

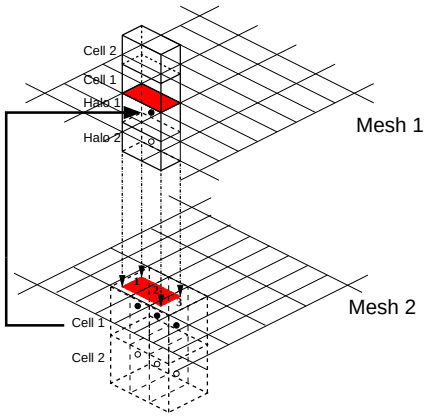

(a) First layer of halo cells (mesh 1)

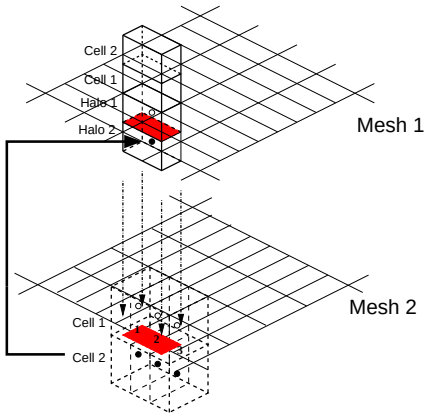

(b) Second layer of halo cells (mesh 1)

Figure 2: Sliding-plane algorithm employing 'direct' interpolation. The cell face is projected on the sliding-mesh interface. The cell-face overlap determines the interpolation weight for each of the donor cells.

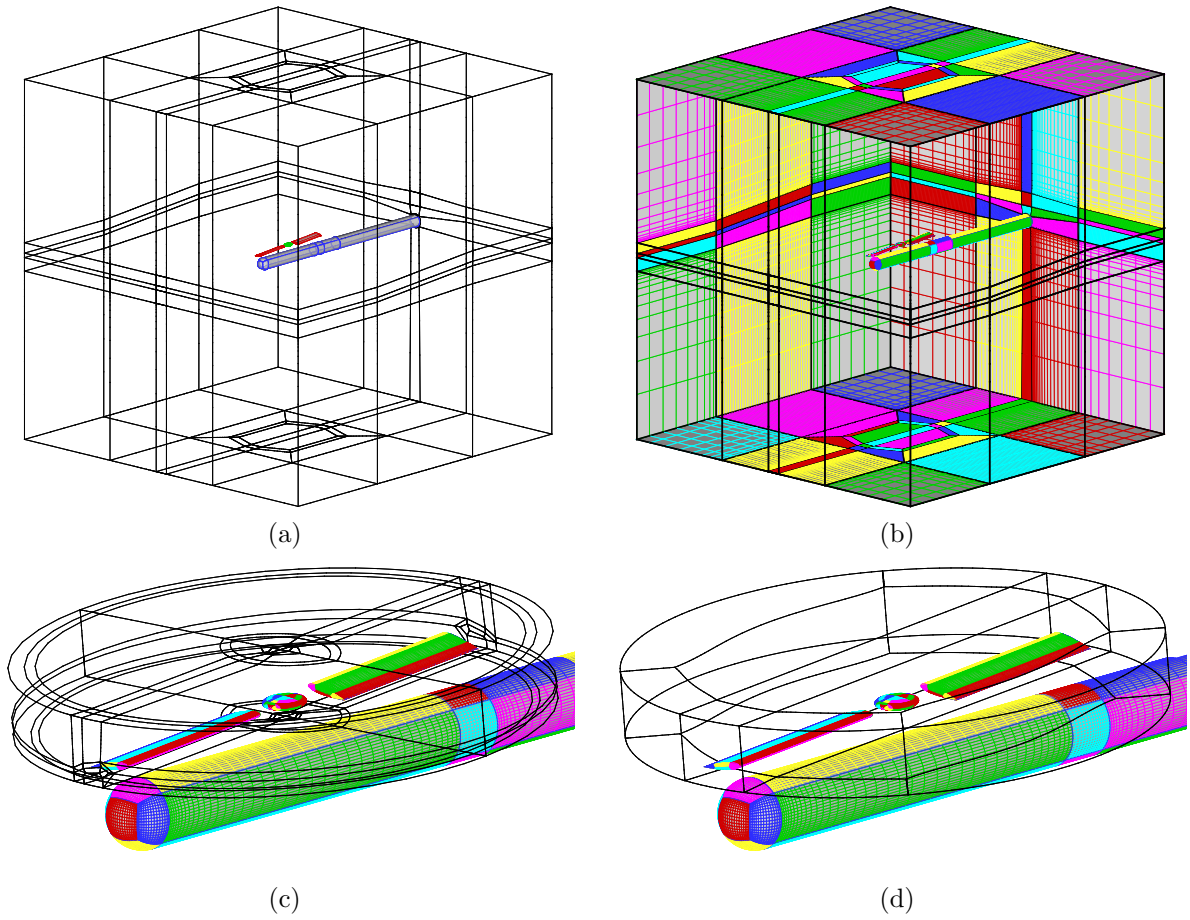

Figure 3: GeorgiaTech test case. The two-bladed teetering rotor is mounted above an idealised airframe with cylindrical shape. The boundary surface and block boundaries along these surface are shown in (a), while (b) shows the surface mesh. The rotor grid outer surface forms a cylindrical drum (c) placed within a matching drum-shaped cavity in the background mesh (d).

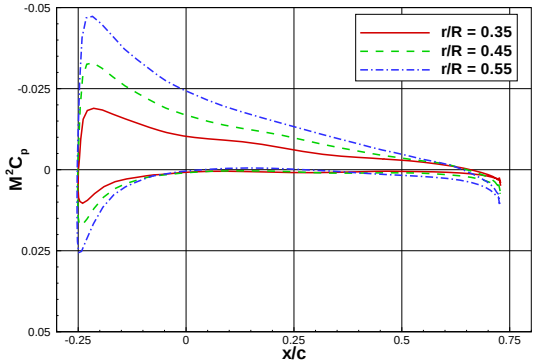

(a) $\psi = 0^o$, inboard

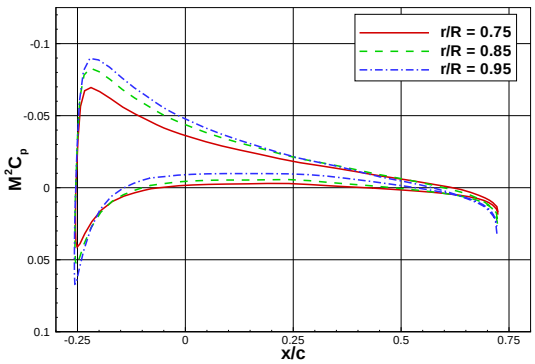

(b) $\psi = 0^o$, outboard

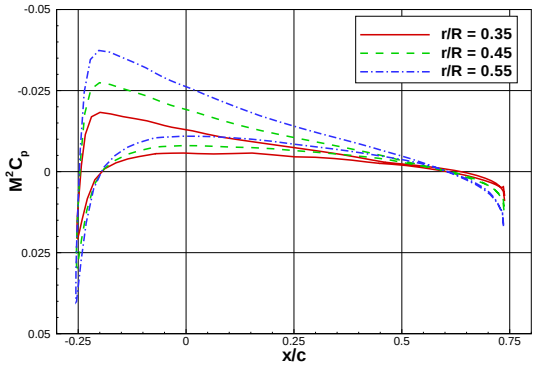

(c) $\psi = 90^o$, inboard

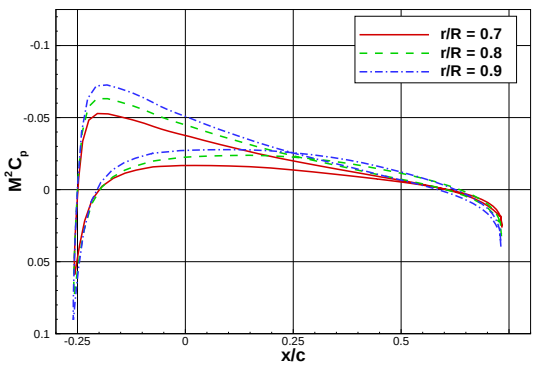

(d) $\psi = 90^o$, outboard

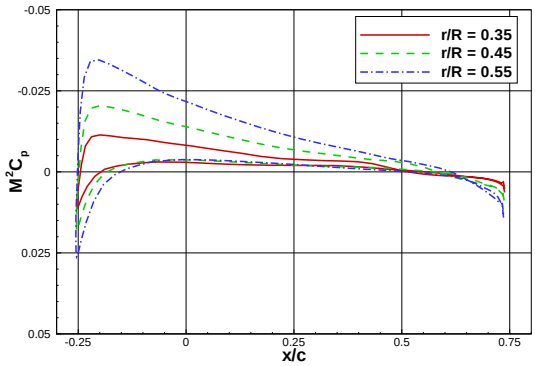

(e) $\psi = 180^o$, inboard

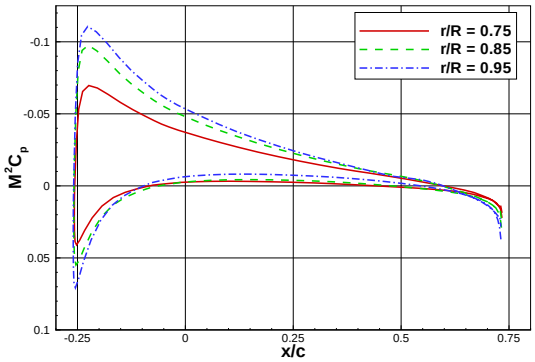

(f) $\psi = 180^o$, outboard

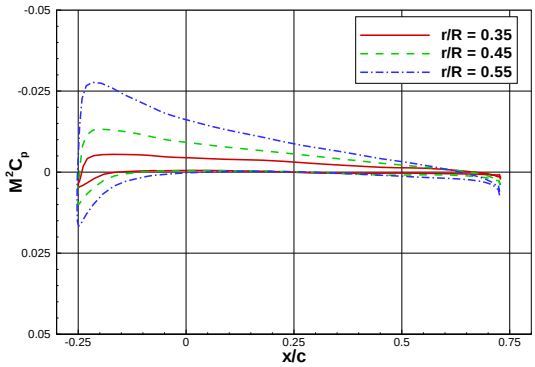

(g) $\psi = 270^o$, inboard

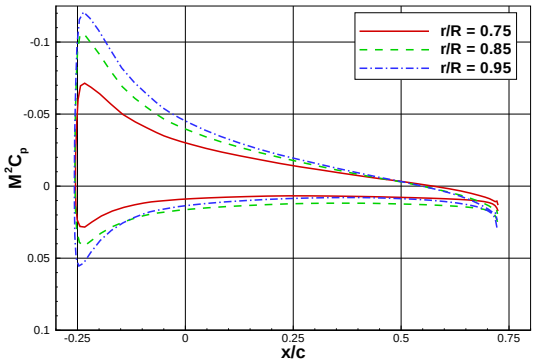

(h) $\psi = 270^o$, outboard

Figure 4: GeorgiaTech test case ($\mu = 0.10$, $C_T = 0.0090$). Chordwise surface pressure distribution for 6 spanwise stations at different rotor azimuths.

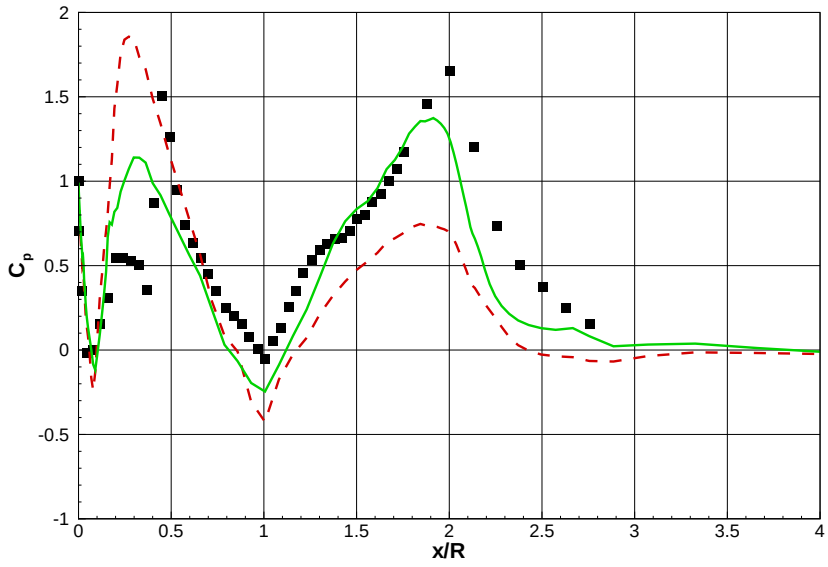

Figure 5: GeorgiaTech test case ($\mu = 0.10$, $C_T = 0.0090$). Revolution averaged pressure along the crownline of the cylindrical body. CFD results with and without flapping are compared with experimental data.

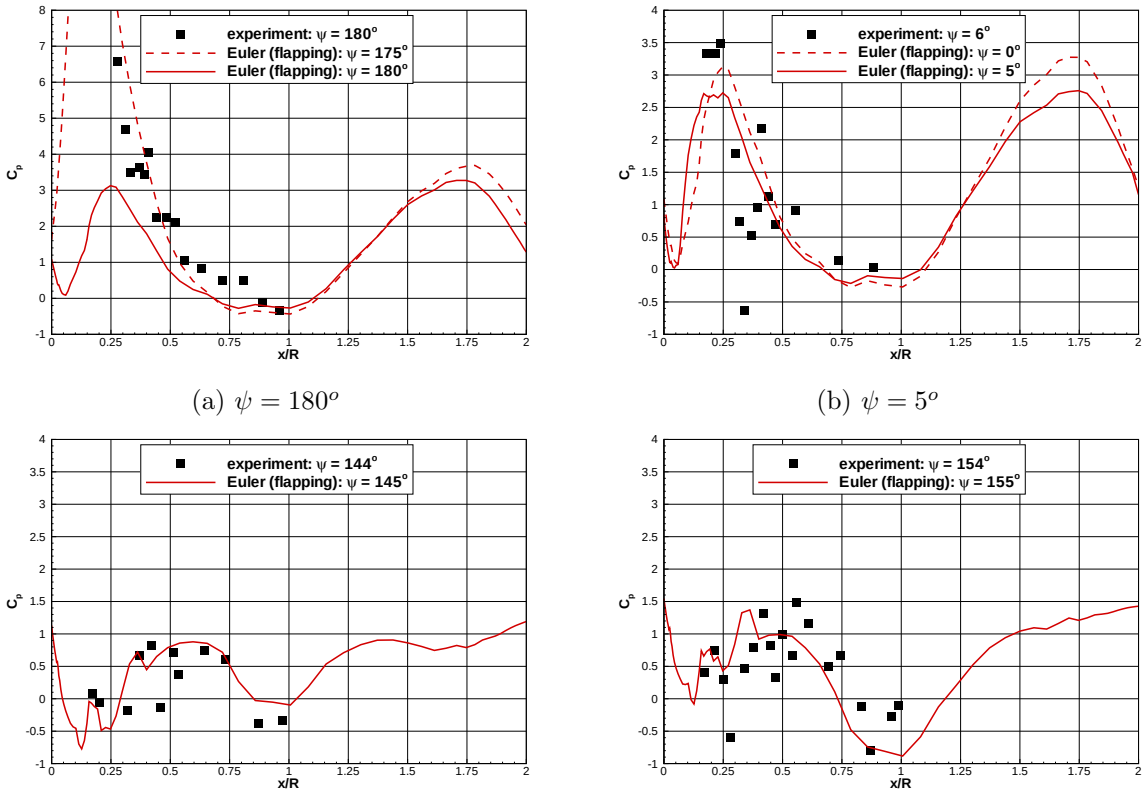

(a) $\psi = 180^o$ (b) $\psi = 5^o$

(a) $\psi = 145^o$ (b) $\psi = 155^o$

Figure 6: GeorgiaTech test case ($\mu = 0.10$, $C_T = 0.0090$). Instantaneous pressure along the crownline of the cylindrical body for different rotor azimuths.

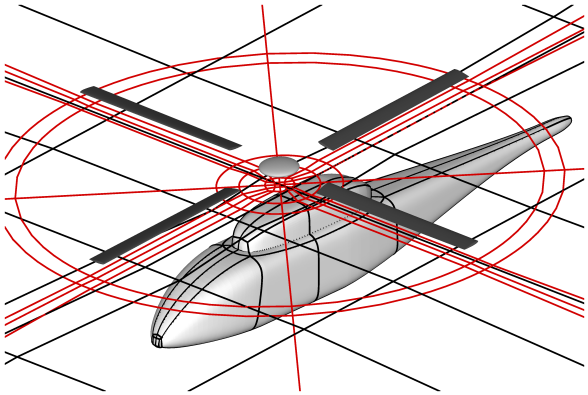

(a) ROBIN configuration and sliding-plane interface

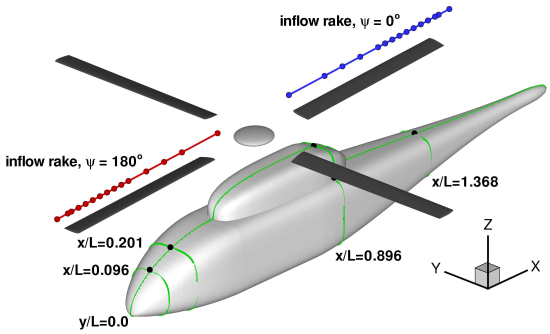

(b) Pressure tap and inflow measurement locations

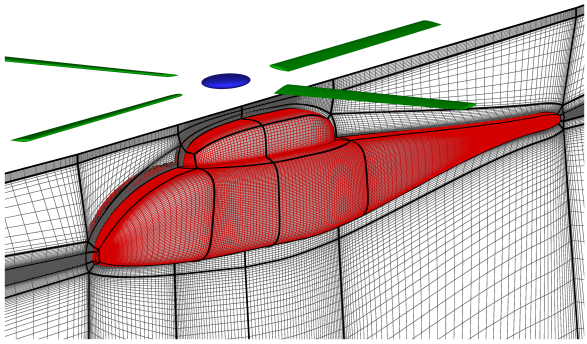

(c) Fuselage and symmetry plane mesh

Figure 7: ROBIN configuration used in the present CFD study. The wind tunnel supports for the floor-mounted fuselage and the roof-mounted rotor are omitted. (a) sliding-mesh interface is located 1.0 blade chord below the rotor disk. (b) location of pressure taps and inflow measurements used in the present work.

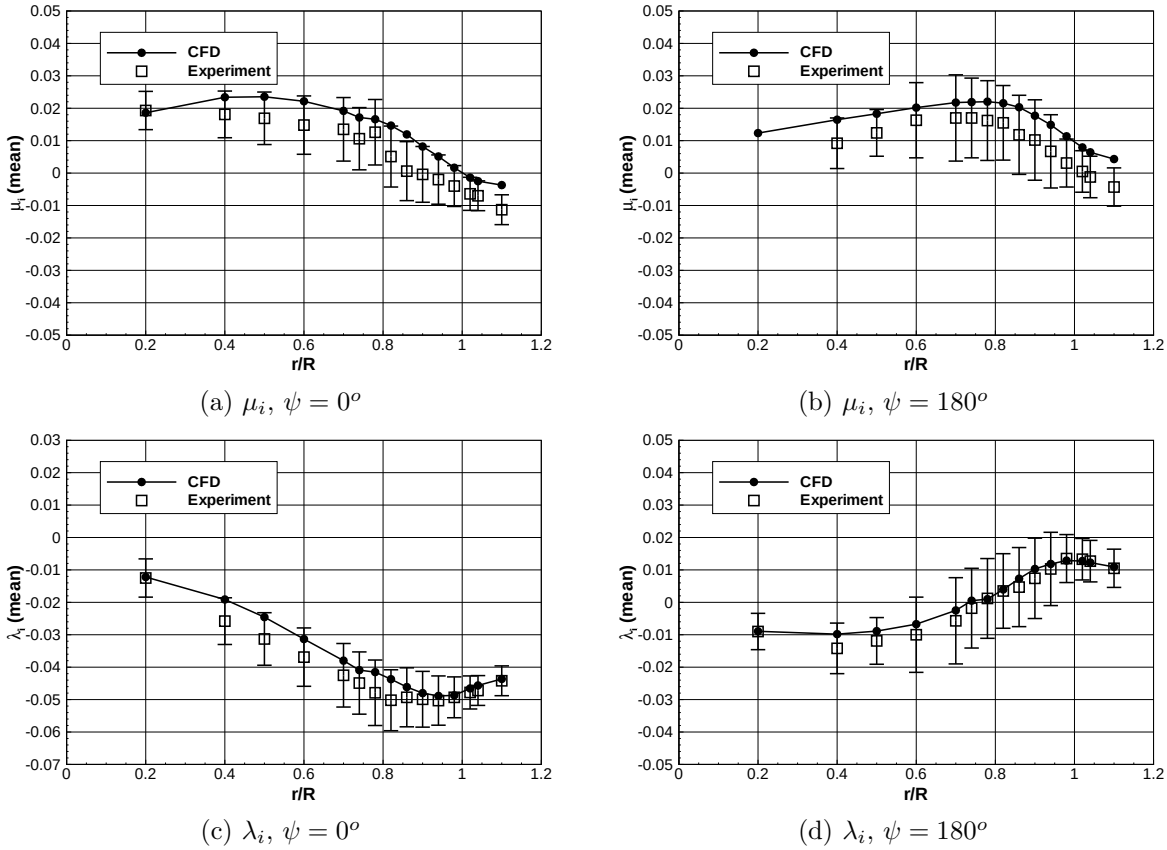

(a) μ_i, $\psi = 0^o$ (b) μ_i, $\psi = 180^o$

(c) λ_i, $\psi = 0^o$ (d) λ_i, $\psi = 180^o$

Figure 8: Robin rotor-fuselage test case ($\mu = 0.15$). In-plane (μ_i) and normal (λ_i) velocity ratios at 0^o (a,c) and 180^o (b, d) azimuth angles. The velocity was extracted above the rotor disk plane at $z/c = 1.1$. The thrust coefficient was $c_T = 0.0065$, $M_{tip} = 0.51$, advance ratio $\mu = 0.15$

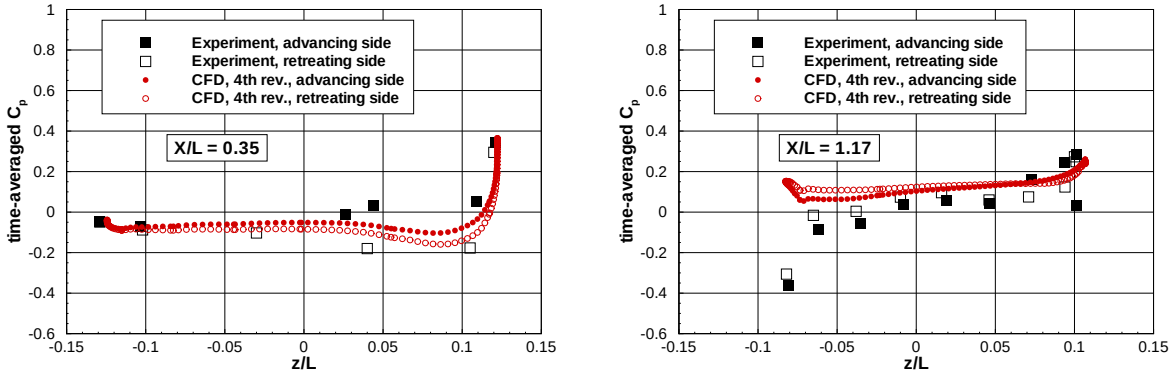

Figure 9: Robin rotor-fuselage test case ($\mu = 0.15$). Time-averaged surface pressure coefficient. Thrust coefficient $c_T = 0.0065$, $M_{tip} = 0.51$, advance ratio $\mu = 0.15$

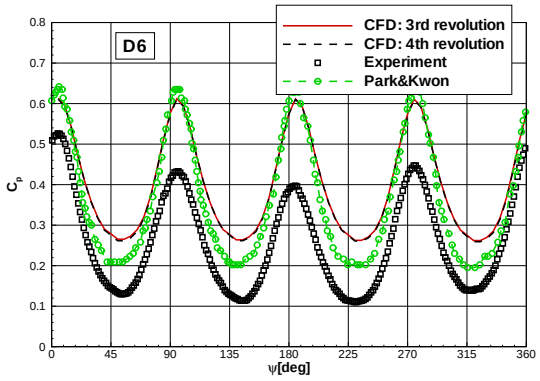

(a) centreline, x/L = 0.096

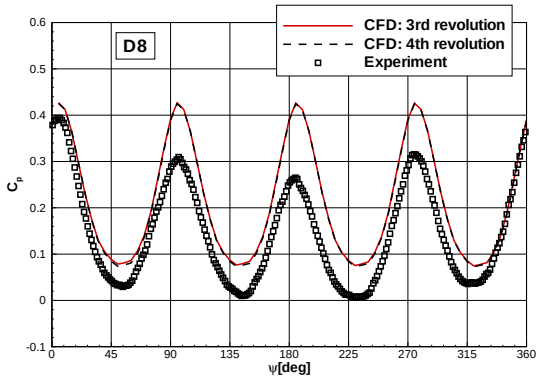

(b) centreline, x/L = 0.201

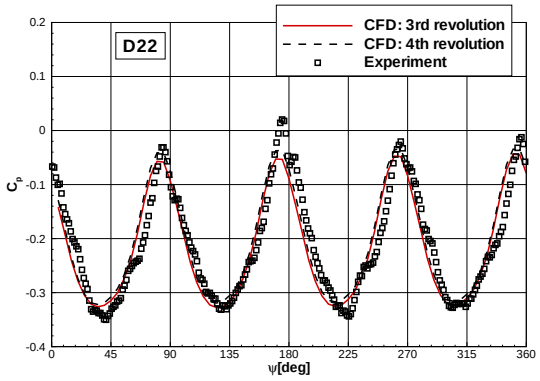

(c) centreline, x/L = 0.896

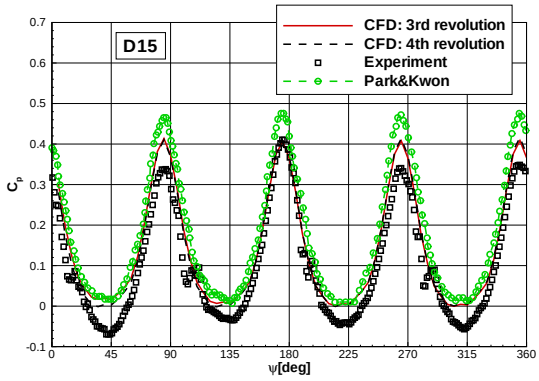

(d) centreline, x/L = 1.368

Figure 10: Robin rotor-fuselage test case ($\mu = 0.15$). Centreline surface pressure distribution for ROBIN test case.

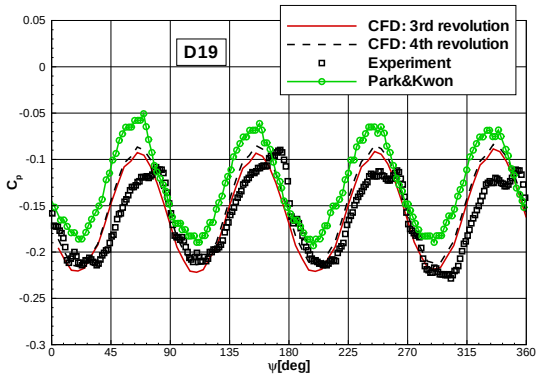

(a) x/L = 0.896, y/L = -0.07, z/L = 0.125

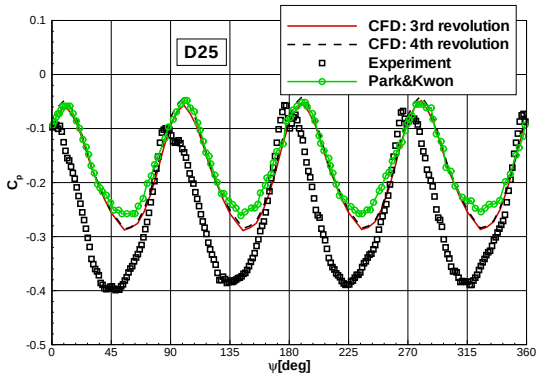

(b) x/L = 1.368, y/L = 0.07, z/L = 0.125

Figure 11: Robin rotor-fuselage test case ($\mu = 0.15$). Surface pressure in probes left and right of the fuselage fairing for ROBIN test case.

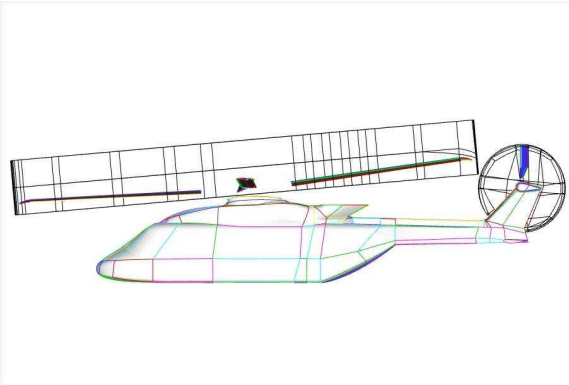

(a) Geometry and sliding planes

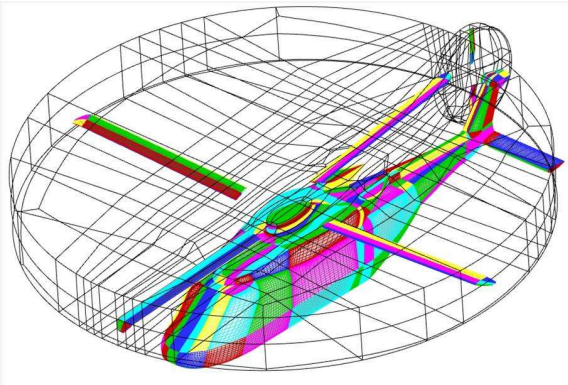

(b) Surface mesh and sliding planes

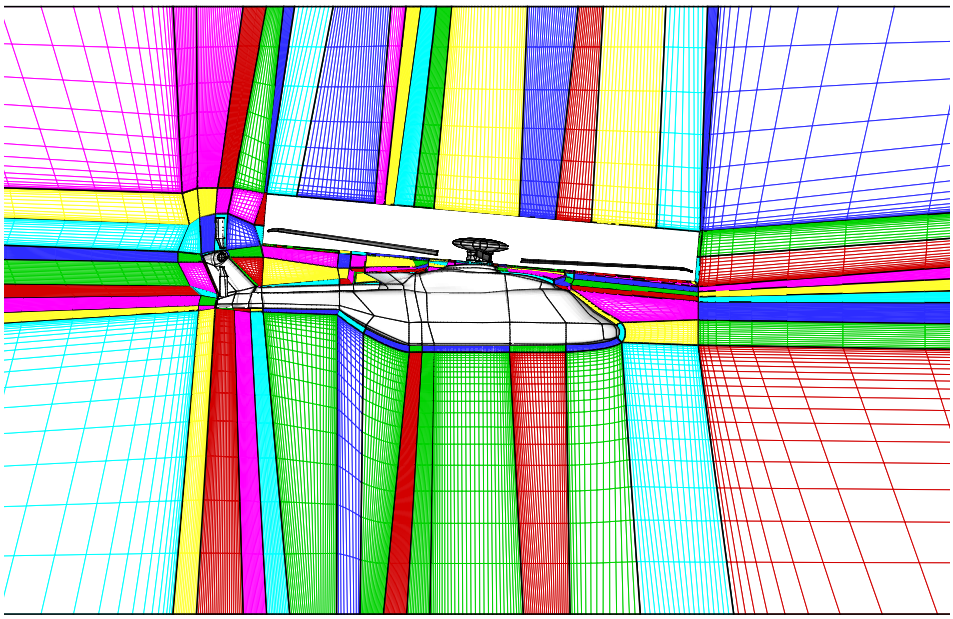

(c) Mesh in $y = 0$ plane

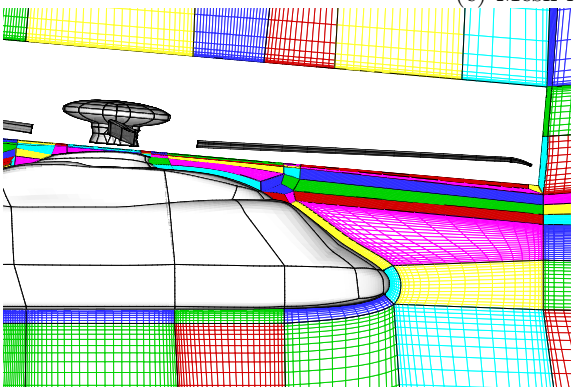

(d) Zoom of nose region of mesh in $y = 0$ plane

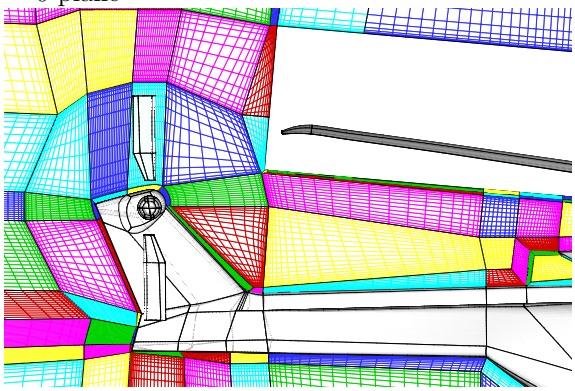

(e) Zoom of tail region of mesh in $y = 0$ plane

Figure 12: GOAHEAD full helicopter geometry. (a-b) the main and tail rotors are placed within drum-shaped sliding-plane interfaces. (c-e) The mesh in the $y = 0$ plane is shown, which does not constitute a symmetry plane. The rotor meshes are not shown for clarity. The mesh has 3786 blocks and $27 \cdot 10^6$ cells. (a) global view of mesh, (b) detail of mesh in nose region, (c) close-up of mesh in tail region.

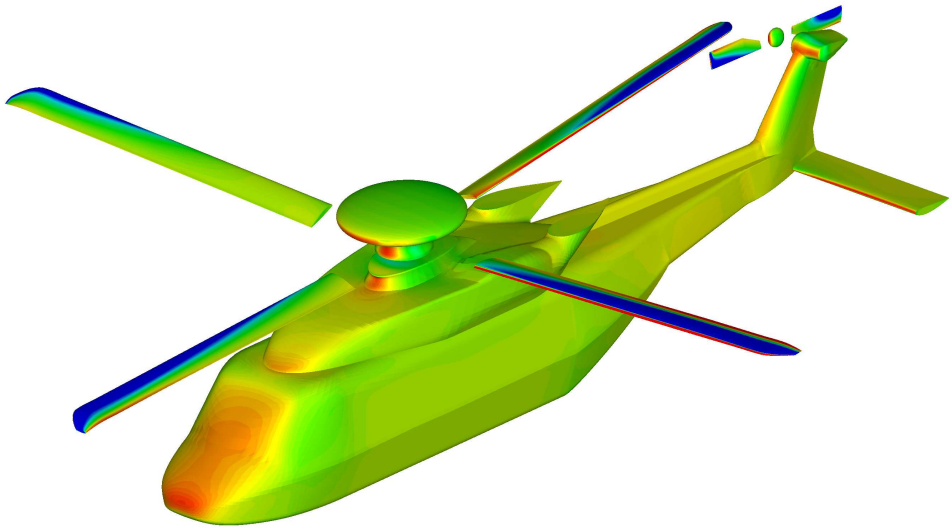

(a) Surface pressure coefficient at $\psi = 90^o$

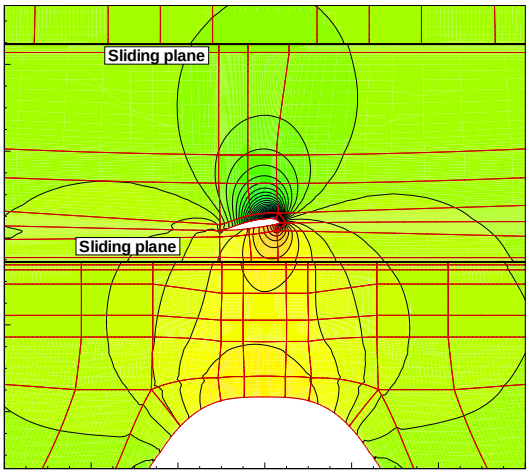

(b) main rotor-fuselage interaction

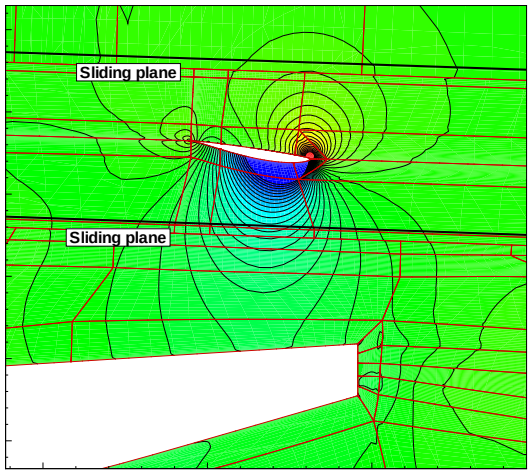

(c) tail rotor-fin interaction

Figure 13: GOAHEAD full helicopter geometry. Economic cruise condition. Instantaneous pressure coefficients are shown. (a) instantaneous surface pressure coefficient at main rotor azimuth 90^o, (b) main rotor-fuselage interaction, $x = 0.75$ cross section (approx. mid span of blade), (c) tail rotor fin interaction, $z = 0.775$ cross-section, at base of fin.